Spatiotemporal dynamics of multiple shear-banding events for viscoelastic micellar fluids in cone-plate shearing flows

Laura Casanellas[a,b,1,*], Christopher J. Dimitriou[b,2], Thomas J. Ober[b,3], Gareth H. McKinley[b,**]

[a] *Departament d'Estructura i Constituents de la Matèria, Universitat de Barcelona, Av. Diagonal 645, 08028 Barcelona, Spain*
[b] *Hatsopoulos Microfluids Laboratory, Massachusetts Institute of Technology, 77 Massachusetts Av., Cambridge, Massachusetts, USA*

Abstract

We characterize the transient response of semi-dilute wormlike micellar solutions under an imposed steady shear flow in a cone-plate geometry. By combining conventional rheometry with 2-D Particle Image Velocimetry (PIV), we can simultaneously couple the temporal stress response with time-resolved velocimetric measurements. By imposing a well defined shear history protocol, consisting of a stepped shear flow sweep, we explore both the linear and nonlinear responses of two surfactant solutions: cetylpiridinium chloride (CPyCl) and sodium salicylate (NaSal) mixtures at concentrations of [66:40] mM and [100:60] mM, respectively. The transient stress signal of the more dilute solution relaxes to its equilibrium value very fast and the corresponding velocity profiles remain linear, even in the strongly shear-thinning regime. The more concentrated solution also exhibits linear velocity profiles at small shear rates. At large enough shear rates, typically larger than the inverse of the relaxation time of the fluid, the flow field reorganizes giving rise to strongly shear-banded velocity profiles. These are composed of an odd number of shear bands with low-shear-rate bands adjacent to both gap boundaries. In the non-linear regime long transients (much longer than the relaxation time of the fluid) are observed in the transient stress response before the fluid reaches a final, fully-developed state. The temporal evolution in the shear stress can be correlated with the spatiotemporal dynamics of the multiple shear-banded structure measured using RheoPIV. In particular our experiments show the onset of elastic instabilities in the flow which are characterized by the presence of multiple shear bands that evolve and rearrange in time resulting in a slow increase in the average torque acting on the rotating fixture.

Keywords: Wormlike micelles, Shear banding, Elastic instabilities, Particle Image Velocimetry

1. Introduction

Wormlike micellar solutions constitute a canonical class of fluids for the study of experimental and theoretical non-Newtonian fluid dynamics [1]. These surfactant solutions have been extensively employed during the last decades for scientific purposes since Rehage and Hoffmann [2] showed that, at small shear rates, they behave according to the Maxwell constitutive equation with a single relaxation time. Surfactant molecules are amphiphilic, with a hydrophilic head and a hydrophobic tail. When dissolved in water, the formation of micelles is energetically favorable above a critical micellar concentration (CMC). This concentration is low for wormlike micelles. Through the addition of a counterion, the ionic strength of the hydrophilic head, which controls the morphology of aggregation in the amphiphilic molecule, is weakened, and the formation of cylindrical (or wormlike) micelles is induced. Some of the most commonly used species, at suitable concentrations and temperature, are the cetylpiridinium chloride/ sodium salicylate system (CPyCl/NaSal) [2, 3, 4, 5, 6, 7], as well as cetyltrimethylammonium bromide with counterion consisting of either sodium nitrate (CTAB/$NaNO_3$) [8, 9, 10, 11, 12, 13], sodium salicylate (CTAB/NaSal) [14, 15, 16], or potassium bromide (CTAB/KBr [17]). A comprehensive survey of wormlike micellar solutions exhibiting different rheological behaviors is provided by Lerouge and Berret [18]. Above the overlap concentration the long flexible wormlike micelles start to overlap forming entanglements [19]. In this semi-dilute regime the entanglements between flexible wormlike micelles form a mesoscopic network which is primarily responsible for the viscoelastic response of the fluid. Wormlike micelles are also known as *living polymers* because, unlike polymeric solutions, wormlike chains have the ability to constantly reassemble after breakage [20]. Micellar solutions are used in a wide range of practical applications and are frequently present in detergents, emulsifiers, encapsulants or lubricants [21].

Shear banding refers to the ability of a fluid to locally separate into two or more coexisting macroscopic bands with markedly different local viscosities under an imposed shearing deformation. Complex fluids exhibiting long relaxation times and strong shear thinning are likely to exhibit shear banding [1]. In particular, several species of wormlike micelles have emerged as model systems to understand shear-banding phenomena [1, 22, 18]. Shear-banding fluids are commonly characterized by a nonmonotonic underlying constitutive response. The material response exhibits a linear viscoelastic regime at small shear rates, but becomes unstable above a critical shear rate, $\dot{\gamma}_c$. Above this critical value the macroscopic rheological response of the

*Corresponding author
**Principal corresponding author
Email addresses: laura.casanellas@espci.fr (Laura Casanellas), chrisd@mit.edu (Christopher J. Dimitriou), tober@seas.harvard.edu (Thomas J. Ober), gareth@mit.edu (Gareth H. McKinley)
[1]Present address: Laboratoire Physique et Mécanique de Milieux Hétérogènes, ESPCI, 10 rue Vauquelin, 75231 Paris Cédex 05, France; Laboratoire Matière et Systèmes Complexes, Université Paris 7 Diderot, 10 rue Alice Domon et Léonie Duquet, 75205 Paris Cédex 13, France
[2]Present address: Nike Inc. Polymers R&D 13630 SW Terman Rd. Beaverton, OR 97005, USA
[3]Present address: School of Engineering and Applied Sciences, Wyss Institute for Biologically Inspired Engineering, Harvard University, Cambridge, MA 02138, USA

solution (as measured in a bulk rheometric device) strongly shear thins and the flow curve exhibits a pronounced shear stress plateau. The fluid locally reorganizes into a new heterogeneous configuration composed of different localized shear-rate bands. These bands can support different local shear rates, that coexist at a common shear stress: a low shear rate band $\dot{\gamma}_1$ (which coincides approximately with the beginning of the stress plateau), and a high shear rate region $\dot{\gamma}_2$ (coincident with the end of the stress plateau). The average (imposed) shear rate of the fluid in the rheometer is related to $\dot{\gamma}_1$ and $\dot{\gamma}_2$ through the lever rule

$$\dot{\gamma} = (1 - f)\dot{\gamma}_1 + f\dot{\gamma}_2, \tag{1}$$

where f and $(1 - f)$ are the volume fractions of the high and low-shear-rate bands. Different bands have different microstructural organization, corresponding to different degrees of alignment of the wormlike micelles under shear. These microstructural variations can be detected using birefringence measurements [23, 24].

Britton and Callaghan [5] first observed the formation of shear bands using Nuclear Magnetic Resonance (NMR) in a cone-plate geometry under *steady* shear for a wormlike micellar solution composed of CPyCl/NaSal at a concentration of [100:60] mM. They documented three different shear bands arranged normal to the velocity gradient direction, with one high-shear-rate band at the center of the gap and two low-shear-rate bands adjacent to each of the boundaries. Fluctuations of the interface between adjacent shear bands were also reported [25]. In particular, slow migration of the interface (on time scales of many seconds) was observed and attributed to stress relaxation. Later development of rapid 2D NMR velocimetry enabled the visualization of fast transients in the fluid response [26]. An investigation of the spatiotemporal flow dynamics of CTAB surfactant solutions in a Taylor-Couette (TC) cell, using rapid NMR and additional ^{2}H spectroscopy measurements was recently provided in Brown and Callaghan [27]. Most visualization experiments performed subsequently have focused on Taylor-Couette (TC) geometries. Salmon et al. [28] as well as Lettinga and Manneville [29] performed steady flow experiments with similar semi-dilute wormlike micellar solutions using dynamic light scattering and ultrasonic velocimetry. They showed that in the TC geometry typically only two different steady shear bands form: a high-shear-rate band adjacent to the moving cylinder and a low-shear-rate band adjacent to the stationary one. These different flow organizations (i.e. whether we observe the formation of two or three shear bands) in different devices presumably arise from the different interplay between boundary conditions and the intrinsic stress gradient imposed by the flow geometry [30].

Further understanding of the dynamics in micellar Taylor-Couette flow was developed by Lerouge et al. [10], Fardin et al. [13, 31] using a shear-banding wormlike micellar solution (CTAB/$NaNO_3$ [0.3:0.405] M). The expected shear-banded flow profiles composed of two concentric bands were recovered and the lever rule was satisfied all along the stress plateau. However they observed the destabilization of the high-shear-rate band leading to the formation of *viscoelastic* vortices distributed along the cylinder axis, which displayed a rich variety of spatiotemporal flow patterns. At even higher shear rates a transition from a laminar to an

elastically turbulent state (comparable to the elastic turbulence state previously reported by Groisman and Steinberg [32] for polymeric solutions) was described, even though inertial effects were always negligible. They expanded the parameter regime studied by systematically tuning the surfactant concentration of the solutions [33], and elucidated the interplay between elastic instabilities and shear-banding. More recently, they tested an even more diluted *non-shear-banding* wormlike micellar solution (CTAB/$NaNO_3$ [0.1:0.3] M) [34]. In this lower viscosity system inertial effects become significant, and this enables a probing of the interplay between fluid inertia and viscoelasticity, that leads to the formation of inertio-elastic vortices.

Careful monitoring of the transient rheological response of complex fluids has been used extensively by researchers as a sensitive probe of the onset of elastic flow instabilities. In an early study Ken Walters and colleagues reported a protracted slow increase in the measured torque for a polyacrylamide Boger fluid undergoing start-up of steady shear in a cone-plate device [35]. This apparent shear thickening in the fluid's viscometric response is now known to be a direct signature of a purely elastic instability in a torsional shear flow. Transient or start-up flows of wormlike micellar solutions have also been widely studied in different flow geometries [3, 4, 36] and flow visualization has been carried out using different techniques [9, 37, 16, 11]. In particular, using ultrasound velocimetry Bécu et al. [38] observed oscillations of the interface between adjacent shear bands in a TC cell. Such oscillations were found to induce the nucleation of a second high-shear-rate band next to the stator, which formed intermittently in time. Wall slip also played a relevant role in their experiments. Transient spatiotemporal features of the shear-banded profiles were also reported by López-Gónzalez et al. [39] as well as Miller and Rothstein [40] using CPyCl/NaSal micellar systems in the TC geometry. The latter authors attributed those observations to the formation of multiple metastable (transient) shear bands. Hu and coworkers [41, 42] studied the kinetics and mechanism of shear banding for different surfactant concentrations using Particle Tracking Velocimetry (PTV), but also focused primarily on TC and plate-plate geometries. Further experiments have been performed by Boukany and Wang [43] using PTV to characterize the nonlinear flow behavior of a CTAB/NaSal solution under various modes of shear (startup, creep and LAOS). They observed a broad diversity in the fluid non-linear response including wall slip, interfacial slip (attributed to local chain disentanglement and scission), as well as localized shear-banding. Visualization of shear flows of CTAB/NaSal solutions using PTV was also achieved by Yamamoto et al. [44] in a plate-plate device. Their velocity measurements displayed shear-banded profiles with three different bands and a time-dependent location of the band interface.

In Dimitriou et al. [45] we showed using Particle Image Velocimetry (PIV) that a CPyCl/NaSal solution at [100:60] mM sheared in a cone-plate geometry could exhibit shear-band formation under *oscillatory* shear flows when the applied deformation rate and amplitude exceeded a shearing threshold, typically $Wi = \lambda\omega/\theta_0 > 1$, where the relaxation time of the fluid is $\lambda = 1.45$ s, θ_0 is the cone angle, and ω the angular velocity. The velocity profiles displayed three bands, agreeing with the results of Britton and Callaghan [5, 25] obtained for the same geometry. The PIV measurements showed that in this oscillatory

time-varying flow there was a rather smooth variation of the shear rate across the gap. The shear-banded profile could be satisfactorily fitted with a sigmoidal function with four adjustable fitting parameters. The onset of shear-band formation in large amplitude oscillatory shear (LAOS) was accompanied by an increase in the ratio of the third to the first-order Chebyshev coefficients (e_3/e_1 and ν_3/ν_1), as a result of the appearance of higher harmonics in the periodic stress response of the fluid. The important role of different experimental configurations was also discussed in this earlier study. It was shown that the addition of a transparent adhesive polymer film at the top surface prevented slip at the surface and enhanced shear-band formation in the bulk. The incorporation of an external lens, which was useful to keep the meniscus flat, was also evaluated. It was concluded that it was preferable not to use a lens, since it exacerbated the onset of secondary flows which can also complicate analysis of shear banding in other strongly shear-thinning materials such as monodisperse polymer melts [43, 46].

In the present work we report a systematic study of the transient response of two semi-dilute micellar systems composed of CPyCl/NaSal at two different surfactant concentrations, under imposed steady shearing flow in a cone-plate geometry using a Rheo-PIV experimental setup. The imposed shear flow consists of a stepped ramp composed of increasing applied shear rates which enables us to characterize both the linear and nonlinear responses of the micellar solutions. In the first part of Sec. 2 we briefly report on the rheological characterization of both the semi-dilute [66:40] mM and more concentrated [100:60] mM surfactant solutions. In the second part of this section we describe the Rheo-PIV setup that was used to perform the experiments. Special attention is given to the new imaging configuration that has been developed, which allows the visualization of the fluid motion through a beveled surface at the edge of the upper rotating plate. This new configuration also enables recording of velocimetric data at different radii, thereby elucidating possible spatial variations of the velocity profiles along the radial coordinate. In a previous iteration of the Rheo-PIV device, image distortion was likely to occur at moderate shear rates due to slight edge irregularities at the air-fluid meniscus. The new design bypasses these issues. In Sec. 3 we first report the experimental results obtained for the more diluted shear-thinning solution (Sec. 3.1). Next, we present the results obtained for the concentrated and shear-banding solution under a shear flow of equivalent strength and analyze the transient response in different time windows (Sec. 3.2.1); in Sec. 3.2.2 we study the spatial structure of the shear-banded velocity profiles that form in the non-linear flow regime, and in Sec. 3.2.3 we focus on the dynamical rheological behavior that occurs in conjunction with these profiles. Finally, the main conclusions of this work are discussed in Sec. 4.

2. Materials and Methods

2.1. Wormlike micellar solutions

The surfactant solution utilized here consists of cetylpiridinium chloride (CPyCl from Alfa Aesar, $m_0 =$ 358 g/mol) and sodium salicylate (NaSal from Alfa Aesar, $m_0 = 160.1$ g/mol) dissolved in de-ionized water, with a concentration [100:60] mM. A second solution of CPyCl/NaSal with a considerably lower concentration of surfactant and salt [66:40] mM (but with the same relative ratio of CPyCl to NaSal set to 1.66, and still in the semi-dilute regime) was also used in order to explore the role of shear thinning and elasticity on the observed flow patterns. Both fluids have been studied in extensional flow using the cross slot geometry by Haward and McKinley [47]. Both solutions were prepared by adding carefully weighed amounts of the two chemicals to de-ionized water and mixing for 24 hours at room temperature. The solutions were stored in a dark chamber to avoid any possible sample degradation caused by ambient light [48].

The majority of the rheometric tests were performed using a controlled-stress rheometer AR-G2 (TA Instruments, New Castle, DE). Complementary results over a wider range of shear stress were obtained using a controlled-stress DHR-3 rheometer (TA Instruments, New Castle, DE) and a microfluidic rheometer m-VROC (Rheosense, San Mateo, CA).

Figure 1 shows the characterization of the linear viscoelasticity of both fluids. In the first panel we show the viscoelastic moduli G' and G'' obtained by performing a frequency sweep at a constant deformation of $\gamma_0 = 10\%$. In the bottom panel we show the Cole-Cole response for both solutions. The linear viscoelasticity of the both fluids is well described by a single-mode Maxwell model at low frequencies (shown with solid lines in the figure) [2, 7]. At T=25°C the relaxation time for the [100:60] mM solutions is $\lambda = 1.45$ s and the shear modulus $G_0 = 27.6$ Pa [45]. As described by Haward and McKinley [47], when the surfactant concentration is reduced both the relaxation time and zero-shear viscosity of the micellar solution rapidly decrease. Furthermore, by decreasing the surfactant concentration the viscoelastic behavior of the solution progressively deviates from a purely single-mode Maxwellian behavior. Note that for the dilute [66:40] mM fluid the Maxwell model is fitted only before the crossover in G', G''. The shear modulus provided by the fit for this more dilute system is $G_0 = 3.2$ Pa, and the relaxation time $\lambda = 0.63$ s. Although the solution exhibits a clear Maxwellian behavior in the terminal regime, at higher frequencies the single-mode Maxwell model is not able to accurately reproduce the experimental measurements of the moduli for this solution (as shown in Fig. 1) indicating substantial contributions from higher relaxation modes. We thus prefer to compute an average relaxation time from the inverse of the crossing frequency (ω_c) of G' and G'', which leads to $\lambda = 0.3$ s. In Tab. we report a summary of the rheological values obtained for both micellar solutions at 25.0°C.

In Fig. 2 we show the steady shear flow curve measured at this same temperature for the [100:60] mM solution. It exhibits an initial linear regime at small shear rates with constant viscosity, $\eta_0 = 39$ Pa·s.

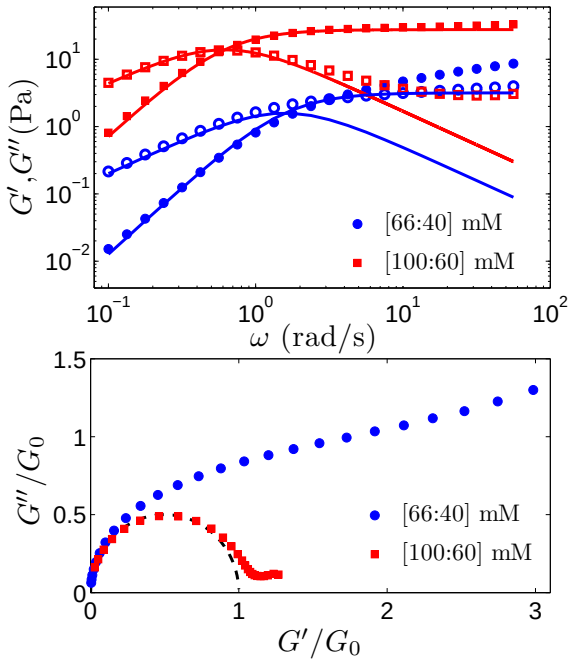

Figure 1: Top: Storage (filled symbols) and loss moduli (empty symbols) versus angular frequency for the CPyCl/NaSal [66:40] mM and [100:60] mM solutions, measured with the DHR-3 rheometer with a cone-plate geometry (aluminum cone of 2° and 50 mm diameter), at $T = 25.0°$C. Experimental results and analytical fitting curves (solid lines) based on a single mode Maxwell model. Bottom: Cole-Cole plot of the variation in the loss modulus $G''(\omega)$ with the storage modulus $G'(\omega)$.

At shear rates larger than a critical shear rate $\dot{\gamma}_c \simeq 0.6$ s^{-1}, corresponding to a Weissenberg number of $Wi = \lambda\dot{\gamma} = 0.87$, the solution strongly shear thins and the flow curve exhibits a pronounced shear stress plateau, $\tau_{plateau} \simeq 15$ Pa. Above this critical shear rate, viscometric flow becomes unstable against the formation of different shear bands [20, 22, 1, 31]. These results are consistent with previous studies that used identical or comparable wormlike micellar solutions [2, 49, 23, 7, 36, 24].

For increasing shear rates the flow curve exhibits a local maximum in stress just above the critical shear rate (shown in the inset of Fig. 2). This local maximum in stress is only observed under controlled-rate

Concentration (mM)	λ (s)	G_0 (Pa)	η_0 (Pa·s)
[66 : 40]	0.3 ± 0.1	3.2 ± 0.5	3 ± 1
[100 : 60]	1.45 ± 0.1	27.6 ± 0.5	39 ± 1

Table 1: Rheological properties of the wormlike micellar CPyCl/NaSal solutions obtained at 25.0°C from steady and oscillatory data after fitting the single-mode Maxwell model.

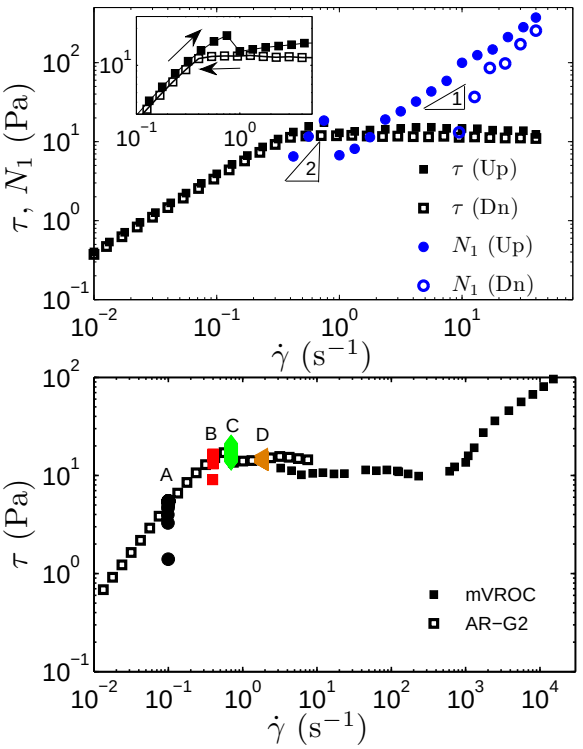

Figure 2: Top: Shear stress and first normal stress difference for the CPyCl/NaSal [100:60] mM solution measured at increasing (up) and decreasing (dn) shear rates using the DHR-3 (aluminum cone of 2° and 60 mm diameter). Inset: zoom of the hysteretic region for the shear stress close to the onset of shear banding. Bottom: Extended flow curve measured for the same fluid. At low shear rates we have used the AR-G2 and at large shear rates the m-VROC microfluidic rheometer. In both panels the temperature is set to 25.0°C. In capital letters are shown the shearing values corresponding to the Rheo-PIV experiments.

conditions and reflects the metastability of this region of the flow curve [50]. The shear rate sweeps were performed by allowing a maximum time of 180 s at each shearing point to make sure that the fluid response was quasi-steady and initial transients had faded away. The local maximum in shear stress is reduced by allowing this time to increase and would eventually disappear in the limit of infinite sampling time. When decreasing the shear rate, there was no sign of a stress maximum but a constant stress value was observed all along the plateau. This hysteretic behavior, as well as the nonmonotonicity of the steady flow curve, with a manifest stress-plateau, are two signatures of the underlying shear-banding behavior of the solution [50].

The measurements of the first normal stress differences, performed with the DHR-3 rheometer, are also shown in Fig. 2. At small shear rates N_1 displays a quadratic dependence with the applied shear rate, which decreases in the nonlinear regime to an almost linear dependence. This behavior for N_1 is in accordance with previous published results obtained by Pipe et al. [36] for the same micellar system, but is not well described by many constitutive models.

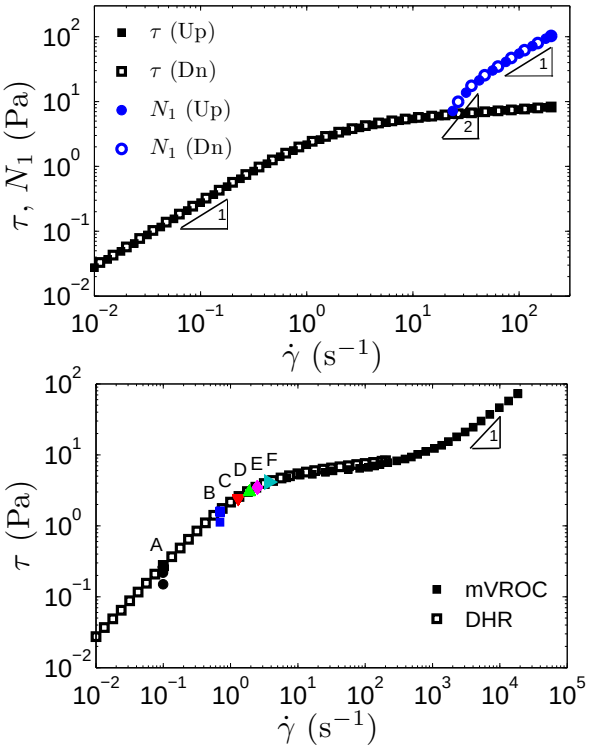

Figure 3: Top: Flow curve and normal stress differences for the dilute solution [66:40] mM measured at increasing and decreasing shear rates using a DHR-3 rheometer (aluminum cone of 2° and 50 mm diameter). Bottom: Extended flow curve for the dilute solution. The data acquisition in the range of large shear rates has been obtained with a m-VROC rheometer. The temperature is set to 25.0°C. In capital letters are shown the shearing values corresponding to the Rheo-PIV experiments.

The range of shear rates experimentally accessible with a rotational rheometer is limited by edge distortions and foaming appearing at moderate shear rates. We extended this range by using a microfluidic capillary rheometer, m-VROC (Rheosense, San Mateo, CA) [51]. The measurements were performed under imposed flow rate conditions, using a syringe pump. The pressure drop (ΔP) was measured by four in-line pressure transducers distributed along the channel centerline. The shear stress at the walls (τ_w) can be calculated from the pressure drop. For a Newtonian fluid the shear rate at the walls can be directly determined from the imposed volumetric fluid rate. By contrast, in order to take into account the shear thinning of the micellar fluid and derive the *true* shear rate at the walls, we apply the Weissenberg-Rabinowitsch-Mooney correction [51, 24]. In Fig. 2 we superimpose the data obtained with the m-VROC rheometer in the range of large shear rates, to the data obtained with the rotational rheometer at smaller shear rates. We observe that the stress plateau extends over three decades in shear rate, from 0.6 s^{-1} up to approximately 5×10^2 s^{-1}. Note however that there is a considerable reduction (by about 30%) in the value of the stress plateau from that measured with the rotational rheometer when we use the microfluidic device, $\tau_{plateau} \simeq 10$ Pa.

This difference may be caused by a combination of wall slip and non-local effects, which have both been shown to alter the measured flow curve of wormlike micellar fluids [12]. The non-local nature of the flow curve is caused by diffusion of more highly stressed micellar species to regions of lower stress, which can be significant because the small gap width in the microfluidic device (99.6 μm) results in large spatial gradients in the stress field. In this regime the flow is no longer truly determined by the local conditions, since the diffusion gives rise to stress boundary layers [52], which are typically on the order of $\delta \sim 10$ μm, thereby altering the resulting stress vs. shear rate relationship. This has been documented for this CPyCl/NaSal system by Ober et al. [24]. Numerical simulations of the pressure driven flow in a narrow slit with the VCM model (which captures the coupling between stress and diffusion) show very similar trends [50].

The steady flow curve measured for the diluted solution using both the torsional and microfluidic rheometers is shown in Fig. 3. The solution exhibits a linear response for shear rates lower than $\dot{\gamma}_c \simeq 2$ s^{-1}, with a constant shear viscosity of $\eta_0 = 3$ Pa·s. Above this critical shear rate the fluid strongly shear thins. A fundamental difference between the two surfactant solutions is that whereas the flow curve of the more concentrated system exhibited a marked stress plateau (a mechanical signature of shear banding [18]), the shear stress for the more diluted solution always increases monotonically with applied shear rate. This monotonicity in the flow curve strongly suggests that the kinematics in the cone-plate geometry for the [66:40] mM system should be spatially homogeneous. By measuring the flow curve at increasing and decreasing shear rates (Fig. 3), we detected no hysteresis between the two trajectories for the diluted system. Very good overlap in both the measured shear stress and first normal stress difference when ramping up and down the shear rate is observed. The absence of hysteresis for the more dilute solution is another indication that shear banding does not play a major role in the deformation kinematics of the less concentrated system.

In Haward and McKinley [47], the authors tested different micellar systems of various surfactant and counterion concentrations, in order to unravel the influence of fluid formulation on the extensional properties and onset of elastic instabilities in a cross-slot geometry. They observed that the flow bifurcated from a steady symmetric configuration to a steady asymmetric configuration, with the appearance of a birefringent strand, followed by a second transition to a 3D time-dependent flow, as the Weissenberg number was steadily increased. The degree of shear thinning of the different micellar solutions they studied was quantified using a dimensionless shear-thinning parameter $S \equiv (1 - \eta_c/\eta(\dot{\gamma}))$ (first introduced by Sharma and McKinley [53]), where $\eta_c \equiv \partial\tau/\partial\dot{\gamma}$ is a tangent viscosity (or *consistency*) [54]. This parameter can be rewritten in terms of the slope of the flow curve (plotted in a log-log scale) as $S = (1 - \partial \ln \tau/\partial \ln \dot{\gamma})$. Using three different dimensionless numbers (Re, Wi and S) they constructed a complete flow stability diagram and evaluated the role of fluid inertia, fluid viscoelasticity and level of shear thinning in controlling the stability boundaries. We set out to explore here the role of changing the degree of shear thinning (S) on the shear flow of wormlike micellar fluids in a cone-plate configuration. In our case fluid inertia is negligible, since the Reynolds number $Re \ll 1$ for the flow of both micellar solutions. Thus we focus on the $S - Wi$ projection

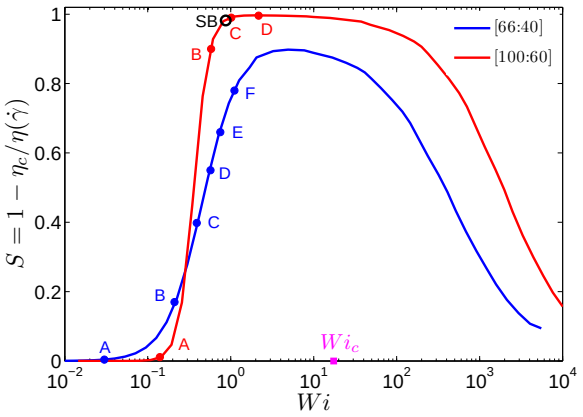

Figure 4: Shear-thinning parameter S versus Weissenberg number Wi measured for both micellar systems. In capital letters are shown the values corresponding to the Rheo-PIV experiments (the same notation as in Figs. 2 and 3 has been used). More details are provided in the text. SB stands for the onset of shear banding, and Wi_c indicates the onset of the purely elastic instability for a constant viscosity fluid with no shear thinning (S=0).

in which the interplay between fluid viscoelasticity and shear thinning becomes relevant. In Fig. 4 we show the evolution in $S(\dot{\gamma})$ expected for both solutions, in terms of Wi. The shear-thinning parameter has been calculated by first fitting a Carreau-Yasuda model [19] to our flow curve data (following the same procedure described in detail in Haward and McKinley [47]; details are given in the supporting information).

By keeping the Weissenberg number fixed, different classes of viscoelastic fluids can be investigated just by increasing S. The limit $S \equiv 0$ corresponds to an ideal elastic liquid with constant viscosity, as predicted by the Oldroyd-B model for example. The intermediate range for which $0 < S < 1$ accounts for weakly shear-thinning fluids. Note that for strongly shear-thinning fluids $\partial \ln \tau / \partial \ln \dot{\gamma} = n$ (where $n - 1$ is the exponent of the power-law decay of the viscosity), so that $S = 1 - n$. The limit of $S \to 1$ describes a shear-banded or yielding fluid, where $n \simeq 0$.

At small Wi, the more concentrated [100:60] mM system (represented in red in Fig. 4) displays a linear flow curve and thus $S \simeq 0$; as Wi increases the solution strongly shear thins and S rapidly grows; above the critical shear rate for the onset of shear banding (shown with a black circle in the figure) S approaches the maximum value of unity, which corresponds to the stress plateau in the flow curve where $\eta \propto \dot{\gamma}^{-1}$. The diluted [66:40] system (shown in blue in Fig. 4) also exhibits an initial linear regime where $S \simeq 0$, for a very small range of Weissenberg numbers. The shear-thinning parameter smoothly increases, for increasing Wi, up to $S \simeq 0.9$ but never reaches values close to unity. By comparing the computed trajectories for the two solutions in the $S - Wi$ space, it becomes clear that we can explore different parts of this phase space and we show in the following that a very significant level of shear thinning seems to be required in order to observe the onset of shear banding, or even of elastic flow instabilities.

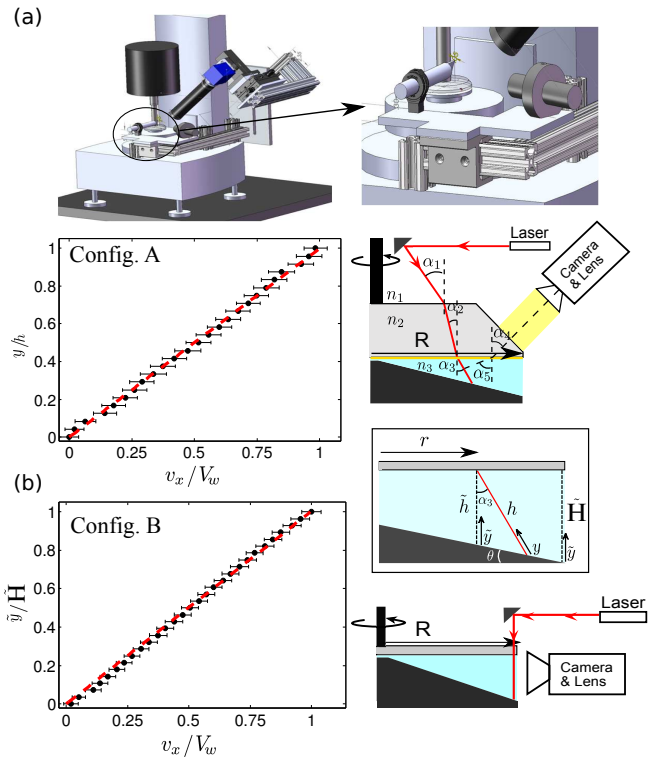

Figure 5: Schematic view of the Rheo-PIV experimental setup is shown on the right-hand side. In the new configuration (a) the imaging was achieved through the tilted surface of the upper plate. In the old configuration (b) it was achieved through the fluid meniscus. The cone-plate configuration is not shown to scale. The actual cone angle is only 4° so that the gap $H = R\tan\theta \ll R$. Calibration curves obtained in both configurations are shown on the left. The vertical position along the gap y, has been made dimensionless by dividing by the gap width. The velocity along the x direction, v_x, has also been made dimensionless by measuring it in units of the velocity of the upper plate, V_w, at the corresponding radial position in each case. The dashed lines are linear fits to the data.

2.2. Rheo-PIV experimental setup

The Rheo-PIV setup used to perform the experiments combined a conventional controlled-stress-rotational rheometer (AR-G2, TA Instruments) with a Particle Image Velocimetry (PIV) technique. This allowed for simultaneous time-resolved rheometric and velocimetric data of the sample as it is sheared. This is the same configuration that Dimitriou et al. [55] used for the study of waxy crude-oil systems and that we used in our previous work [45] in which we characterized the formation of shear bands under Large Amplitude Oscillatory Shear (LAOS). A detailed description of the apparatus was provided in these two previous references.

All Rheo-PIV experiments were performed in a cone-plate geometry consisting of an upper transparent acrylic plate ($R = 25$ mm) covered with a thin adhesive backed polymer film, and a lower aluminum black-anodized cone ($R = 25$ mm, $\theta = 4°$).

Temperature control was achieved using a Peltier plate placed under the bottom surface and was set to

$T = 25.0$ °C in all experiments. The sample, previously seeded with titanium dioxide particles (average size 3μm, and density 4,200 kg/m^3 from TSI Inc.) at a concentration of 0.001 wt % was loaded in the geometry gap. A laser sheet illuminated the sample after being reflected on an inclined mirror and passing through the upper transparent plate. A CCD camera (Matrix vision Bluefox) attached to a macroscopic imaging zoom lens (Edmund Optics Techspec VZM 600i) was used to record the fluid motion, with the frame rate set to approximately 50 frames/s. A schematic view of the Rheo-PIV device is shown in Fig. 5. In previous studies [55, 45] the fluid motion was imaged directly through the fluid meniscus (Configuration B in Fig. 5). Although this imaging configuration enabled us to capture the fluid velocity profile with high spatial resolution, it limited the velocimetric measurements to a single radial location, very close to the edge. Furthermore, slight distortions in the meniscus that appear at moderate shear rates can distort the PIV images. The recording configuration that was designed for the set of experiments presented in this article (configuration A in Fig. 5) records the fluid motion through a beveled and polished surface machined into the upper transparent plate at 45°. The laser and camera were mounted onto a machined aluminum frame that allowed for their radial and angular position to be easily adjusted. A simplified diagram of the imaging configuration, including a sketch of the ray tracing path is provided in Fig. 5. As shown in the figure, in the new configuration (A) the laser sheet enters the upper transparent surface at an angle α_1 to the vertical, and at a radial position r. The angle of incidence can be tuned experimentally by modifying the inclination of the tilted mirror - this was typically set to 30° or smaller. After being refracted through the upper surface, the laser sheet illuminates the sample in a plane tilted at an angle α_3 to the vertical. The angles α_1 and α_3 are related through Snell's law: $n_1 \sin\alpha_1 = n_3 \sin\alpha_3$, where n_1 and n_3 are the refractive indices of the air and the fluid, respectively. The velocity profiles reported in the following sections were measured along the tilted vertical coordinate, y (see diagram in Fig.5). The effective tilted gap width (h) measured along y, at a given radial position r, is related to the *true* gap, $\tilde{h} = r\tan\theta$, through

$$\tilde{h} = h(\cos\alpha_3 - \theta\sin\alpha_3), \tag{2}$$

where the approximation $\tan\theta \simeq \theta$ has been taken into account. Note that in this configuration the theoretical velocity profile measured along the tilted vertical coordinate y preserves its linear dependence with y,

$$v(y) = \frac{\Omega}{\theta} y(\cos\alpha_3 - \theta\sin\alpha_3), \tag{3}$$

where Ω is the angular velocity of the upper plate, and θ the cone angle. Expressed in terms of the dimensionless variables it reads

$$\frac{v(y)}{V_w} = \frac{y}{h}, \tag{4}$$

where $V_w = r\Omega$ is the velocity measured at the upper surface at radial position r. Equation (4) is equivalent to the expression that would be obtained for the velocity profile along the vertical gap ($\tilde{h}$) in configuration

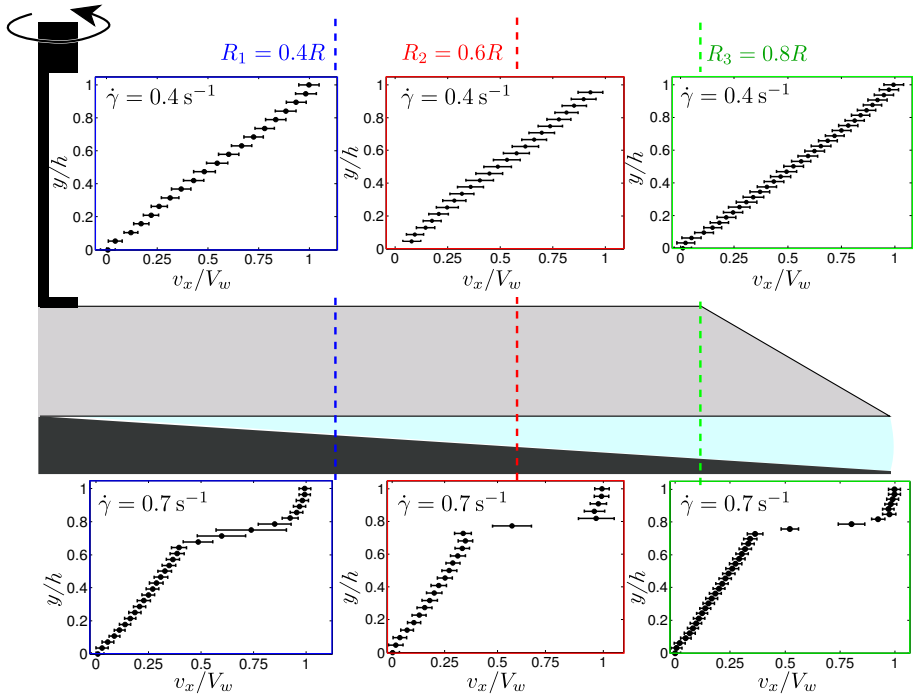

Figure 6: Schematic view (not to scale) of the cone-plate geometry used in the experiments. The velocity profiles measured for the CPyCl/NaSal [100:60] mM solution at different radii (0.4R, 0.6R, and 0.8R) are depicted in the top ($\dot{\gamma} = 0.4\ \mathrm{s}^{-1}$) and bottom panels ($\dot{\gamma} = 0.7\ \mathrm{s}^{-1}$). The velocity has been made dimensionless, in each case, by measuring it in units of the velocity of the upper plate, V_w, at the corresponding radial positions.

B,

$$\frac{v(\tilde{y})}{V_w} = \frac{\tilde{y}}{\tilde{h}}. \tag{5}$$

Figure 5 shows the calibrations performed using a Newtonian mineral oil for an imposed shear rate $\dot{\gamma} = 0.4\ \mathrm{s}^{-1}$. In both configurations the velocity profiles exhibit a linear dependence along the gap width, within experimental error. Linear fits to the experimental data are shown with solid red lines in each figure.

2.2.1. Radial dependence

The new imaging configuration allows velocimetric data to be recorded for a large range of radial positions, $0.4R < r < 0.85R$. Figure 6 shows the velocity profiles measured at three different radii: $r = 0.4R$, $0.6R$, and $0.8R$, and two different applied shear rates: $\dot{\gamma} = 0.4$ and $0.7\ \mathrm{s}^{-1}$ for the more concentrated [100:60] mM CPyCl solution. In the linear viscoelastic regime ($\dot{\gamma} = 0.4\ \mathrm{s}^{-1}$) the velocity profiles are linear (top panels) for all three radial positions, with no significant differences between them. In the nonlinear regime ($\dot{\gamma} = 0.7\ \mathrm{s}^{-1}$) the fluid experiences a non-homogeneous deformation and the velocity profiles display three distinct shear bands. The shape of the shear-banded profile is equivalent for the three positions explored along the radial coordinate. Only small differences regarding the steepness of the velocity profile are

observed. This independence of the shear-banding behavior on the radial coordinate is in good agreement with previous results obtained by Britton and Callaghan [5] who observed the formation of shear bands using magnetic resonance imaging (MRI), which extended uniformly along the cone radius.

The results provided in the remaining sections were all obtained at the particular radial position $r \simeq 0.7R$. In order to make the notation simpler, in the following figures, $h_{r=0.7R}$ is replaced just by H.

2.2.2. Shearing protocol

The experimental protocol consisted of a stepped ramp of increasing applied shear rates, as shown schematically (black squares) in Fig. 7. Steps of $\Delta\dot{\gamma} = 0.6$ s^{-1} were applied for the more diluted solution,

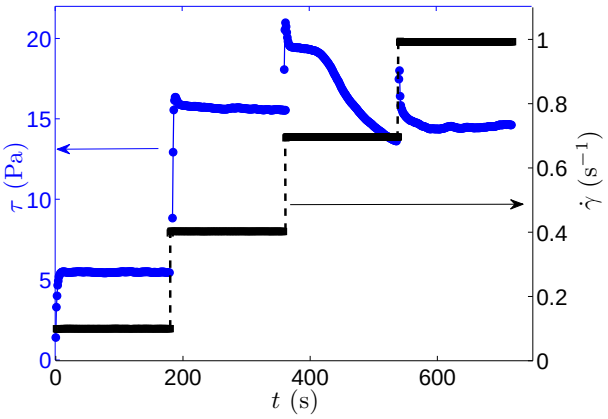

Figure 7: Sketch of the shearing protocol used in the experiments, consisting of a series of steps of increasing shear rates (black squares). The response of the shear stress for the more concentrated system [100:60] mM is shown (blue dots).

setting the smallest applied shear rate at 0.1 s^{-1}. Time intervals of $\Delta t = 180$ s were spent at each shearing rate. The rheometer measures the total torque $\Gamma(t)$ exerted by the fluid and the effective or apparent shear stress (assuming a homogeneous simple shearing flow is given by $\tau = 3\Gamma/2\pi R^3$), shown in blue circles in the figure. In the set of experiments performed for the more concentrated solution the step in shear rate was set to $\Delta\dot{\gamma} = 0.3$ s^{-1}, and typically $\Delta t = 180$ s. In terms of the relaxation time of the fluid, this shearing time corresponds to about 600λ at each step for the more dilute solution, and 124λ for the more concentrated one.

The dimensionless Weissenberg number can be defined in terms of the applied shear rate as, $Wi = \lambda\dot{\gamma}$ where the relaxation time λ for each fluid is determined from linear viscoelastic measurements. The Weissenberg number quantifies the relative strength of the applied deformation and broadly distinguishes the linear fluid response, $Wi < 1$, from the nonlinear regime, $Wi > 1$.

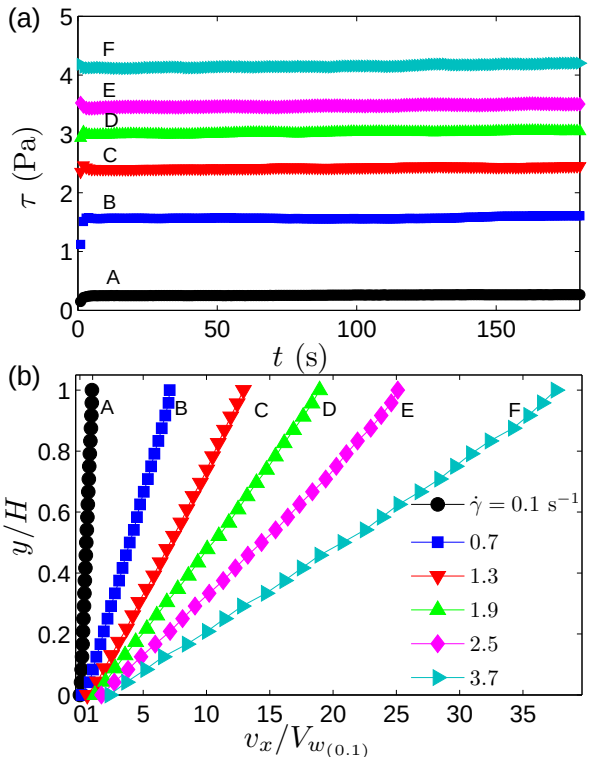

Figure 8: Stress relaxation under imposed steady shear (a) and velocity profiles (b) measured at increasing shear rates for the diluted micellar solution CPyCl/NaSal [66:40] mM. The velocity has been made dimensionless by measuring it in units of the velocity of the upper plate corresponding to an imposed shear rate of $\dot{\gamma} = 0.1$ s^{-1}, V$_w$(0.1).

3. Transient response under an imposed steady shear flow

3.1. Diluted Micellar Solution [66:40] mM

The results obtained for the diluted micellar solution CPyCl/NaSal [66:40] mM are shown in Fig. 8. The solution was sheared with steps of 0.6 s^{-1} from 0.1 s^{-1} up to 3.7 s^{-1} (this upper value being close the largest value experimentally achievable, set by the frame acquisition rate of the camera). The shearing values are also represented in Fig. 3, accompanied by the corresponding capital letter in each case. Inspecting the stress response in Fig. 8(a) we observe that the shear stress in the diluted solution relaxed to its steady state value very fast. For all shear rates explored, and even in the range of $Wi > 1$, the initial transient lasted only for approximately 4 s after the step in shear rate was applied (this time interval was determined by setting a criterion for the relative shear stress variation to be smaller than 1%). This time interval corresponds to about 13 times the relaxation time of the fluid. Accordingly, the velocity profiles measured for the diluted solution (Fig. 8(b)) were linear for all explored shear rates, even for applied shear rates which lay in the shear-thinning regime ($\dot{\gamma} \gtrsim 2$ s^{-1}). Only for the largest shear rates ($\dot{\gamma} = 2.5$, 3.7 s^{-1} in the figure) could a small amount of slip be detected at the bottom stationary surface.

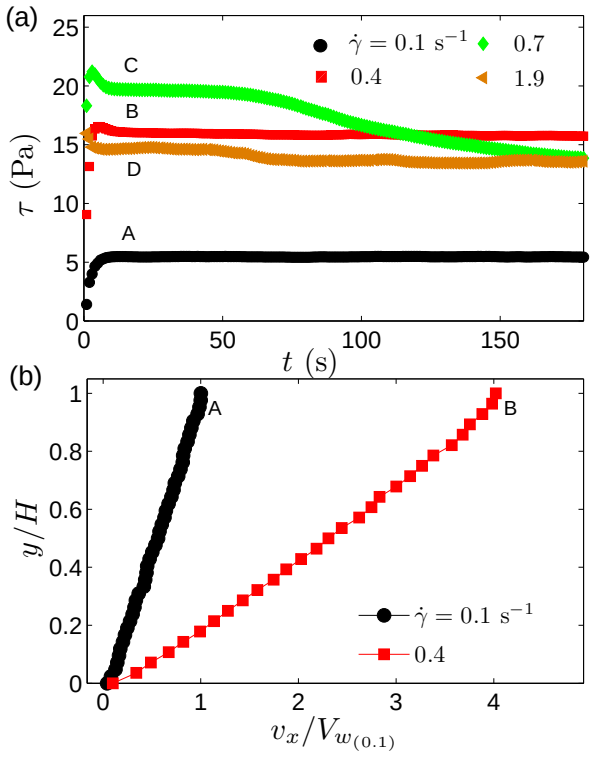

Figure 9: Stress relaxation under imposed steady shear (a) and velocity profiles (b) measured at increasing shear rates for the concentrated micellar solution CPyCl/NaSal [100:60] mM. The velocity has been made dimensionless by measuring it in units of the velocity of the upper plate corresponding to an imposed shear rate of $\dot{\gamma} = 0.1$ s^{-1}, V$_w$(0.1).

As we anticipated in Sec. 2.1, both the monotonicity of the flow curve and the absence of hysteresis seem to indicate that the diluted solution does not undergo a shear-banding transition. Our velocimetric data obtained for this solution further demonstrates that indeed the diluted micellar solution does not shear band in the cone-plate geometry, at least for the range of dimensionless shear rates ($Wi \lesssim 1.1$) explored.

3.2. Concentrated Micellar Solution [100:60] mM

3.2.1. Stress relaxation & elastic instability onset

An analogous set of experiments was performed for the concentrated CPyCl/NaSal [100:60] mM surfactant solution. The fluid was sheared with steps of 0.3 s^{-1} from 0.1 s^{-1} up to 1.9 s^{-1}. The shearing values are also represented in Fig. 2, accompanied by the corresponding capital letter in each case. In panel (a) of Fig. 9 we show the stress relaxation measured for this more concentrated solution and in panel (b) the corresponding velocity profiles. We can distinguish two main regimes; at low shear rates $\dot{\gamma} \lesssim \dot{\gamma}_c$ (corresponding to profiles A and B in Fig. 9) the stress smoothly and rapidly approaches its equilibrium value with a relaxation time interval that is shorter than 10 s (corresponding to about 7λ), in the same way as

observed in Fig. 8(a) for the more diluted system. The corresponding velocity profiles are linear. No slip was detected on either bounding surfaces. For imposed shear rates slightly above a critical value $\dot{\gamma}_c \simeq 0.6 \pm 0.1$ s^{-1} (coincident with the critical shear rate value observed for the onset of shear thinning) the fluid response exhibited much longer transients (profile C). The velocity profiles corresponding to this regime, $Wi \simeq 1$, display pronounced shear bands with sometimes complicated spatiotemporal dynamics (as will be shown in Fig. 10). For imposed shear rates considerably larger than the critical shear rate ($Wi > 1$), the transients in the shear stress response relax considerably faster (profile D). However for this range of applied shear rates the stress response does not reach a final steady regime and slight fluctuations in the stress signal persist over the 180 s of duration of each shearing step, indicative of a time-varying, elastically-unsteady flow. The velocity profiles corresponding to this high shear rate regime are strongly shear banded and will be discussed in detail in Sec. 3.2.2 below.

In order to understand the long transient response of the fluid observed for applied shear rates marginally above the critical shearing value $\dot{\gamma}_c$, we measured the stress response and the corresponding velocity profiles at $\dot{\gamma} = 0.7$ s^{-1} ($Wi = 1.02$) over a time lapse of 900 s (five times longer than the step shearing time used in the previous tests). These results are shown in Fig. 10. The velocity profiles measured after different lapsed periods of time show a complicated temporal evolution of the spatial flow organization along the gap height. Immediately after the step in shear rate is imposed at $t = 0$, the fluid exhibits a significant stress overshoot at timescales comparable to the fluid relaxation ($t \simeq 5\lambda$). After this sudden local maximum, the stress begins a long smooth decay that extends over $60 \lesssim t \lesssim 250$ s. The velocity profiles observed at the beginning of the stress decay ($5 \lesssim t \lesssim 50$ s) exhibit a transient linear behavior (velocity profile A in the figure). This initial linear stage is followed by the reorganization of the fluid flow into different shear bands distributed normal to the velocity gradient direction (profiles B and C). In this stage, the velocity profiles are composed of three different bands, with a high-shear-rate band in the center, and two low-shear-rate bands at the boundaries. These three-banded velocity profiles are consistent with previous results obtained by Britton and Callaghan [5, 25] in a cone-plate geometry under steady shear, and also with our previous work on LAOS [45]. However, the time varying velocity profiles reported in this previous studies exhibited a smoother (less sharply banded) shape than the steady shearing profiles presented here. Approximately 250 s after the initial step shear rate is imposed the stress reaches a quasi-steady state, corresponding to $\tau \simeq 12.5$ Pa. This steady regime persists over the following 250 s. During this time interval the spatial distribution of the shear bands along the vertical coordinate remains almost steady in time (D, E, F). Both the position and width of the shear bands are temporally invariant here.

However, at very long times ($t > 500$ s) the stress slightly increases again by up to approximately $\Delta\tau \simeq 7\%$ (G), measured with respect to the stress value in the quasi-steady regime at intermediate times. It has been argued by Lerouge et al. [11] and Fardin et al. [48] that this stress increase may arise from nucleation and growth of an elastic instability in the strongly shear-banded flow. According to linear

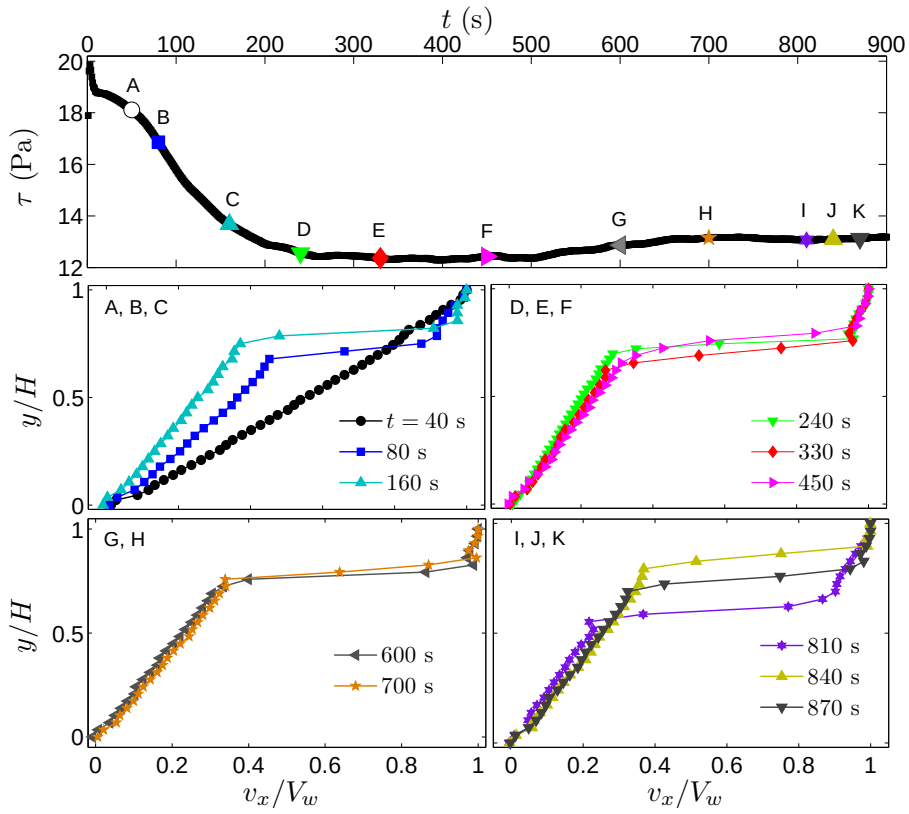

Figure 10: Stress relaxation measured at $\dot{\gamma} = 0.7$ s^{-1} (Wi=1.02) over 900 s for the [100:60] mM solution (top), and velocity profiles measured at different time lapses (denoted with letters in the figure). The velocity has been made dimensionless, in each case, by measuring it in units of the velocity of the upper plate, V_w.

stability analysis [56], a viscometric flow of a viscoelastic fluid (with non-zero N_1) with curved streamlines can become unstable above a critical shearing threshold. This threshold depends on the particular flow geometry. For the case of a spatially homogeneous flow in a cone-plate geometry the instability criterion is given by $\lambda^2\dot{\gamma}^2\theta > 21.17$. Note however, that for a shear-banded flow the spatial dependence of this criterion must be incorporated since the fluid experiences considerably higher shear rates in the spatially localized high shear bands [57]. It is thus reasonable to recompute the criterion using the shear rate corresponding to the high-shear rate band, denoted $\dot{\gamma}_h$ (which will be prone to become unstable more easily) as $\lambda^2\dot{\gamma}_h^2\theta > 21.17$. According to this new definition, the critical shearing value to trigger the onset of elastic instability, and the subsequent development of more complex secondary flows is $\dot{\gamma}_{h,\,crit} = 12$ s^{-1}. As we will see in Sec. 3.2.2 the shear rate measured for the high-shear-rate band is at least of the order of 40 s^{-1}, which clearly exceeds the threshold. Thus, as soon as shear-banded profiles are formed, above $\dot{\gamma}_c = 0.6$ s^{-1}, the elastic instability criterion is satisfied, at least locally. For $t > 500$ s our PIV measurements show that the banded velocity profiles display a notable dynamic *time-dependent* behavior. In Fig. 10 we show the velocity profiles

measured at different times and highlight the dynamical evolution of the banded velocity profile (H, I, J, K). It is clear from the figure that the location of the central high shear-rate region can move significantly upwards and downwards through the gap width, while the sharpness of the velocity profile remains essentially unaltered. We suggest the onset of the elastic instability as the origin of the time-varying motion observed in the high-shear rate band.

3.2.2. Multiple-shear-banded velocity profiles

It was shown in Fig. 9 (a) that for $\dot{\gamma} > \dot{\gamma}_c$, the transients observed in the shear stress response relaxed quite rapidly. This is in comparison with the stress relaxation times observed for applied shear rates that lay close to the critical shear rate for the onset of non-linearities in the flow curve ($\dot{\gamma} \simeq \dot{\gamma}_c$). The corresponding velocity profiles for this range of applied shear rates are always shear-banded, and composed of an odd number of shear bands. The three-banded velocity profiles are well reproduced by the functional form proposed in Dimitriou et al. [45]:

$$v(y) = V_w \left[s \left(\frac{y}{H} \right) + \frac{(1-s)}{2} \left(1 + \tanh \left(b \frac{(y - y_b)}{H} \right) \right) \right]. \quad (6)$$

This function has four fitting parameters: V_w is the velocity at the upper wall; y_b is the mid-position of the high-shear-rate band; b measures the sharpness of the velocity profile; the parameter s is the ratio of the shear rate of the low-shear-rate bands adjacent to the top and bottom surfaces ($\dot{\gamma}_l$, where the subscript l stands for *low*) to the applied shear rate ($\dot{\gamma} = V_w/H$); the ratio of the high-shear-rate band ($\dot{\gamma}_h$, where the subscript h stands for *high*) to the applied shear rate can be expressed in terms of these fitting parameters as $\dot{\gamma}_h/\dot{\gamma} = (s + b(1-s)/2)$. In Fig. 11 (top) we show, as an example, the velocity profile measured at an imposed shear rate of $\dot{\gamma} = 1.9$ s^{-1}. In red we depict the fit obtained using the functional form of Eq. 6. The shear rate value provided by the fit for the low-shear-rate band is $\dot{\gamma}_l = 0.3$ s^{-1}, which coincides reasonably well with the shear rate at the beginning of the stress plateau ($\dot{\gamma}_1$). The value for the high-shear-rate band provided by the sigmoidal fit is $\dot{\gamma}_h \simeq 40$ s^{-1}, which is considerably lower than the shear rate corresponding to the end of the stress plateau ($\dot{\gamma}_2$). Note however that the value obtained for the high shear-rate-band is close to the largest shear rate that could be resolved with our experimental setup, which is intrinsically limited by the spatial resolution of the camera and the cross-correlation algorithm of the PIV software. In order to test whether the measured velocity profile would be compatible with a high-shear-rate band with a shear rate value of $\dot{\gamma_h} = \dot{\gamma}_2$, we have superimposed in Fig. 11 the shear-banded velocity profile computed by restricting the high shear rate to $\dot{\gamma}_h \simeq 500$ s^{-1} (and keeping $\dot{\gamma}_l \simeq 0.3$ s^{-1}). We observe that this second fit (depicted with a dashed blue line in the figure) is also able to accurately reproduce the experimentally measured velocity profile, within experimental error. Thus, a shear-banded profile with $\dot{\gamma}_h \simeq \dot{\gamma}_2$ would be compatible with our experimental results.

In some experiments, specially when applied steps in shear rate were $\Delta\dot{\gamma} > 0.5$ s^{-1}, wall slip occurred at the upper moving surface. When slip was present the formation of bulk shear bands was normally prevented.

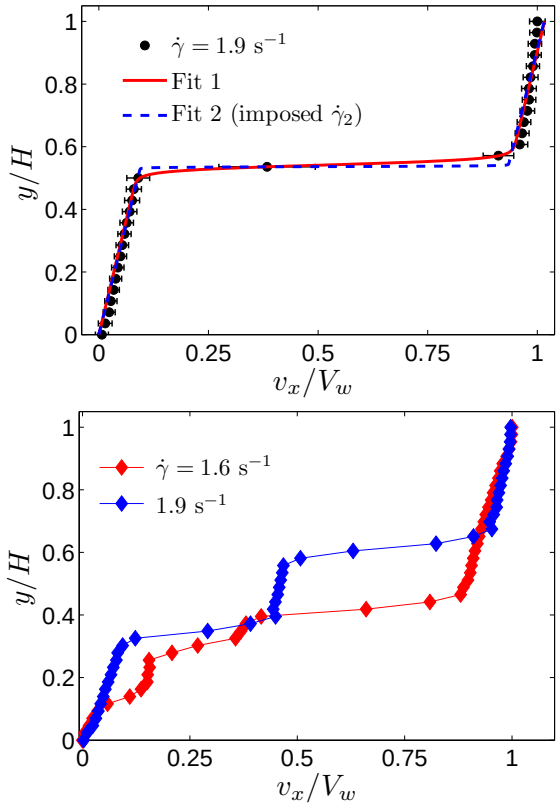

Figure 11: Nonlinear velocity profiles obtained for the concentrated micellar solution [100:60] mM. Top: Three-banded velocity profile measured at $\dot{\gamma} = 1.9$ s^{-1}. The red and blue solid lines are fits to the experimental data (more details are provided in the text). Bottom: five-banded and seven-banded velocity profiles measured at $\dot{\gamma} = 1.9$ s^{-1} and $\dot{\gamma} = 1.6$ s^{-1}, respectively. The velocity has been made dimensionless, in each case, by measuring it in units of the velocity of the upper plate, V_w.

Occasionally in some experiments, the high shear rate band translated towards the upper bounding surface. As the high shear rate band reached the upper fixture apparent *wall slip* appeared to occur. Note that from our Rheo-PIV measurements, it is difficult to distinguish a high-shear-rate band from wall slip, when the high-shear-rate band is located immediately adjacent to the upper moving surface. The shear rate in this region is so high that the velocity change looks like a discontinuity.

Interestingly, in several transient tests we detected the formation of more than three bands. In particular, five distinct bands were frequently observed. And even, in rare occasions, we observed the formation of seven different shear bands. Note that in all cases the inhomogeneous flow organizes itself in an odd number of shear bands (three, five or seven), with low-shear-rate bands adjacent to the two bounding surfaces. In the bottom panel of Fig. 11 we show two different multiple-banded velocity profiles obtained at $\dot{\gamma} = 1.9$ s^{-1} displaying five bands (blue line) and $\dot{\gamma} = 1.6$ s^{-1}, displaying seven bands (red line).

3.2.3. Spatial fluctuations

In addition to the transient motion of the high-shear rate band across the gap we also found that the number of shear bands changed over the course of the experiment, with extinction or, sometimes even the emergence of new shear bands. When bands merge, one of the high-shear-rate bands fades away reducing the number of shear bands by two (remaining always with at least a three-banded state, since a linear homogeneous profile was never recovered in this regime). The onset of elastic instabilities in the high-shear-rate bands appears to generate strong enough fluctuations in the velocity field to promote the reorganization of the shear-banded flow into a new shear-banded state.

So far we have assumed that the flow remains invariant along the azimuthal coordinate, and we computed the mean velocity profiles accordingly, averaging along this coordinate. This was indeed appropriate for the steady (or quasi-steady) velocity profiles observed in the linear regime and at moderate shear rates. However, once complicated spatiotemporal dynamics for the organization of the shear flow set in, we detected in our measurements the appearance of significant velocity fluctuations along the azimuthal coordinate. These fluctuations arise from the flow perturbations noted above, and are strong enough to promote important changes in the flow organization, diminishing (or incrementing) the number of shear bands. In the top and bottom panels of Fig. 12 we show two particular examples of the velocity fields obtained respectively at $\dot{\gamma} = 1.9$ s^{-1} ($Wi = 2.8$) and $\dot{\gamma} = 1.3$ s^{-1} ($Wi = 1.9$) for the more concentrated [100:60] mM fluid. In the top panel the velocity field is invariant along the azimuthal direction x (i.e. the horizontal direction, in the projection shown in the figure), and three different bands can be distinguished along the vertical coordinate (y). The shear bands can be easily identified by a sharp change in the velocity magnitude (represented with the color code) of the velocity field at $y/H \simeq 0.55$, and on the corresponding velocity profile (averaged along the horizontal coordinate). Note that the width of the high-shear-rate band is comparable to the PIV grid size (corresponding to 12 pixels, or 57 μm). In the bottom panel of the figure the velocity field is more complex, displaying five different shear bands (the velocity discontinuities are located at $y/H \simeq 0.6$ and 0.75). But more importantly, the *interfaces* between contiguous shear bands are not as well defined. This results in a rather smoother shear-banded velocity profile across the gap. In the figure we show, as an example, the velocity profile measured locally at $x/H \simeq 0$. In addition, significant heterogeneities in the velocity magnitude can be observed along the horizontal coordinate in all five bands, notably between $0.5 \lesssim y/H \lesssim 0.8$. Under such conditions, spatial averaging along the azimuthal coordinate should be performed with caution. More detailed investigation of these spatiotemporal dynamics require application of temporally and spatially resolved kinematic techniques (such as ultrasonic velocimetry or rheo-NMR for example [58, 59]).

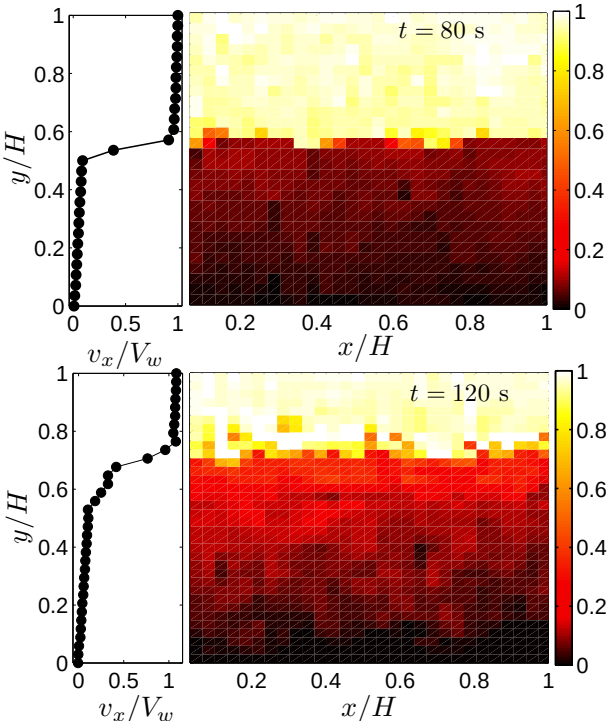

Figure 12: Velocity profiles $v_x(y)$ at $x = 0$ (left) and corresponding 2D velocity fields $v_x(x, y)$ for $0 \leq x \leq H$ and $0 \leq y \leq H$ (right), measured for the more concentrated [100:60] mM solution. Top: velocity field captured after 80 s from the start-up flow set to $\dot{\gamma} = 1.9$ s^{-1}. Bottom: velocity field captured after 120 s from the start-up flow set to $\dot{\gamma} = 1.3$ s^{-1}. The velocity has been made dimensionless, in each case, by measuring it in units of the velocity of the upper plate, V_w and the magnitude is shown by the color bar at right.

4. Conclusions

A systematic study of the formation of shear bands under steady shear flow for two viscoelastic shear-thinning micellar fluids has been performed in a cone-plate geometry. We used a Rheo-PIV setup that allowed us to simultaneously measure the transient shear stress response of the fluid and capture the velocity profile within the sample. A new imaging configuration was developed in the course of these experiments. By recording the fluid motion through a machined and beveled surface on the upper transparent fixture we eliminated optical distortions caused by edge distortions. This new configuration also enabled us to span the radial coordinate and thus measure the velocity profile at different radial locations across the gap. Invariance of the velocity profiles along the radial coordinate was verified, before the onset of time-dependent elastic flow instabilities. We tested two different wormlike micellar solutions of CPyCl/NaSal (with different levels of viscoelasticity and shear thinning). At small applied shear rates ($Wi < 1$) the two solutions displayed linear velocity profiles during steady shearing in the cone-plate device. In the range of $Wi > 1$, the velocity profiles for the more dilute [66:40] mM solution remained linear, even though the solution exhibited

pronounced shear thinning (cf. Fig. 4). These observations, together with the monotonicity and the absence of hysteresis obtained for the flow curve show that this diluted solution is not prone to shear banding, in the range $Wi \lesssim 1.1$. The fact that the flow kinematics observed for this shear-thinning viscoelastic solution remain spatially homogeneous, indicates in turn that the cone-plate shearing flow for this fluid is stable and gives no evidence for the onset of elastically unstable flows. In Fig. 4 we show the critical Weissenberg number (magenta squared dot) for the onset of purely elastic flow instabilities, Wi_c, obtained from the work of Pakdel and McKinley [56], for a cone-plate geometry. Note that this value corresponds to the particular case $S \equiv 0$, for which no shear thinning is considered. The instability criterion will also vary with the degree of shear thinning [60] and typically shear thinning acts to stabilize flows against elastic curved streamlines instabilities.

However different classes of elastic instabilities may also be introduced by the presence of shear thinning. The influence of the degree of shear thinning on the stability of a channel flow of a White-Metzner fluid was theoretically investigated by Wilson and Rallison [61] (the White-Metzner model is a modification of the upper-convected-Maxwell model which takes into account a shear-thinning viscosity as $\eta(\dot{\gamma}) \propto \dot{\gamma}^{(n-1)}$ [19]). Their linear stability analysis showed that in channel flows only viscoelastic fluids with a significant level of shear thinning (with a power-law exponent $n \leq n_c \simeq 0.3$)
were likely to become unstable to flow disturbances. The channel base flow of shear-thinning fluids departs from the parabolic velocity profile, and instead displays a plug-like shape with high-shear-rate regions localized next to the walls. This flow stratification allows for flow reversal in the wall layer, which amplifies streamline perturbations, and triggers a so called *elastic shear-thinning* instability. Moreover, inertio-elastic flow instabilities have also been reported in recent experiments performed by Perge et al. [34] in a TC flow using non-shear-banding but shear-thinning wormlike micellar solution, that develop as a result of the interplay between fluid inertia and viscoelasticity. The experiments we have performed in the cone-plate geometry with the more dilute shear-thinning [66:40] mM solution are restricted to the inertialess regime ($Re < 1$) and lay in a moderate range of shear rates ($Wi \lesssim 1.1$). The findings of Wilson and Rallison [61] in a Poiseuille flow suggest that a significant degree of shear thinning of the fluid is necessary to trigger an elastic shear-thinning flow instability, $S \equiv 1 - n \geq 0.7$. Although we exceed this level of shear thinning for the [66:40] mM solution (the fitting values of a Carreau-Yasuda model for the micellar solutions are provided in the supplementary information) only moderate levels of elasticity are attained. The kinematics are also sufficiently different that it is unclear at present if the cone-plate flow can become elastically unstable for a strongly shear-thinning viscoelastic fluid at $Wi \gtrsim 1$. Only the shear flow for the more concentrated [100:60] mM solution (which displays greater elasticity and an even more pronounced level of shear thinning as shown in Fig. 4) has been shown to become elastically unstable in our experimental results.

The concentrated [100:60] mM solution displayed pronounced shear-banded profiles, in accordance with our previous LAOS tests described by Dimitriou et al. [45]. We found that the dynamics of the shear-

banded profiles depends on the relative distance between the applied shear rate $\dot{\gamma}$ and the critical shear rate $\dot{\gamma}_c$ (determined as the shear rate in the flow curve at which the stress plateau starts). Slightly above threshold, the shear-banded profiles display slow diffusive dynamics associated with coupling between the state of stress and the local velocity and concentration fields [50]. A first transient stage was observed with linear velocity profiles. Three different shear bands, distributed normal to the velocity gradient direction, formed after the initial stress overshoot decayed. The bands remained steady for about 250 s (172λ). After this time interval the high-shear-rate band begins to slowly migrate. This effect is accompanied by a slight increase in the torque signal recorded by the rheometer, which can be interpreted as a signature of the onset of an elastic instability in the steady torsional flow. According to these simultaneous observations, we may view the onset of an elastic instability as the origin for the time-dependent shear-banded velocity profile. Previous results provided by Lerouge et al. [11] for a CTAB/$NaNO_3$ solution in a TC cell, pointed towards the same conclusions. They observed the destabilization of the interface between adjacent shear bands along the vorticity axis, which displayed complicated spatiotemporal dynamics. Simultaneous measurements of the mechanical response in their system also revealed an increase of the apparent shear stress. Observations in both geometries suggest the onset of an elastic instability in the high-shear-rate band.

In our experiments we also observed the formation of more complex velocity profiles consisting of five or even seven shear bands (the number of bands being always an odd number). To our knowledge no comparable shear-banded profiles have been reported before for wormlike micellar systems in cone-plate geometries. Numerical simulations have shown that slow diffusive dynamics of multiply-banded states are predicted to occur in the TC geometry [50]. The experimental results that we provide here, thus, enlarge the phenomenology observed for well-characterized shear-banding wormlike micellar solutions available in the literature, and may inspire future research on understanding the dynamical behavior of shear-banding phenomena and the interaction of shear-banded and elastically unstable flows.

5. Acknowledgements

We acknowledge stimulating discussions with J. Ortín and M. A. Fardin. LC acknowledges ME (Spain) for a fellowship FPU and the financial support received from project No. FIS2010-21924-C02-02, and project No. 2009-SGR- 0014 (Generalitat de Catalunya). TJO was supported by an NSF Graduate Research Fellowship and CJD was supported by the Chevron Energy Technology Corporation. GHM and CJD would like to acknowledge the Chevron-MITEI University Partnership Program for support of RheoPIV studies in complex fluids at MIT.

References

[1] P. D. Olmsted, Perspectives on shear banding in complex fluids, Rheol. Acta 47 (2008) 283–300.

[2] H. Rehage, H. Hoffmann, Viscoelastic surfactant solutions - model systems for rheological research, Molec Phys 74 (1991) 933–973.

[3] J.-F. Berret, D. C. Roux, G. Porte, Isotropic-to-nematic transition in wormlike micelles under shear, J. Phys. II France 4 (1994) 1261–1279.

[4] C. Grand, J. Arrault, M. E. Cates, Slow transients and metastability in wormlike micelle rheology, J.Phys. II France 7 (1997) 1071–1086.

[5] M. Britton, P. Callaghan, Two-phase shear band structures at uniform stress, Phys. Rev. Lett. 78 (1997) 4930–4933.

[6] G. Porte, J.-F. Berret, J. L. Harden, Inhomogeneous flows of complex fluids: Mechanical instability versus non-equilibrium phase transition, Phys. II 7 (1997) 459 – 472.

[7] A. F. Méndez-Sánchez, M. R. López-González, V. H. Rolón-Garrido, J. Pérez-González, L. de Vargas, Instabilities of micellar systems under homogeneous and non-homogeneous flow conditions, Rheol. Acta 42 (2003) 56–63.

[8] E. Cappelaere, R. Cressely, Shear banding structure in viscoelastic micellar solutions, Coll. and Polym. Sci. 275 (1997) 407–418.

[9] S. Lerouge, J. P. Decruppe, Correlations between rheological and optical properties of a micellar solution under shear banding flow, Langmuir 16 (2000) 6464–6474.

[10] S. Lerouge, M. Argentina, J. P. Decruppe, Interface instability in shearbanding flow, Phys. Rev. Lett. 96 (2006) 088301:1–4.

[11] S. Lerouge, M. A. Fardin, M. Argentina, G. Grégoire, O. Cardoso, Interface dynamics in shear banding flow of giant micelles, Soft Matter 4 (2008) 1808–1819.

[12] C. Masselon, J. B. Salmon, A. Colin, Nonlocal effects in flows of wormlike micellar solutions, Phys. Rev. Lett. 1 (2008) 38301:1–4.

[13] M. A. Fardin, B. Lasne, O. Cardoso, G. Grégoire, M. Argentina, J. Decruppe, S. Lerouge, Taylor-like vortices in shear-banding flow of giant micelles, Phys. Rev. Lett. 103 (2009) 1–4.

[14] T. Shikata, H. Hirata, E. Takatori, K. Osaki, Nonlinear viscoelastic behavior of aqueous detergent solutions, J. Non-Newtonian Fluid Mech. 28 (1988) 171–182.

[15] H. Azzouzi, J. P. Decruppe, S. Lerouge, O. Greffier, Temporal oscillations of the shear stress and scattered light in a shear-banding-shear-thickening micellar solution, Eur. Phys. J. E 17 (2005) 507–514.

[16] J. Decruppe, O. Greffier, S. Manneville, S. Lerouge, Local velocity measurements in heterogeneous and time-dependent flows of a micellar solution, Phys. Rev. E 73 (2006) 061509.

[17] O. Radulescu, P. D. Olmsted, J. P. Decruppe, S. Lerouge, J.-F. Berret, G. Porte, Time scales in shear banding of wormlike micelles, Eur. Phys. Lett. 62 (2003) 230–236.

[18] S. Lerouge, J.-F. Berret, Shear induced transitions and instabilities in surfactant wormlike micelles, Springer-Verlag Berlin Heidelberg, 2009.

[19] R. B. Bird, R. C. Armstrong, O. Hassager, Dynamics of Polymeric Liquids Vol. 1, 2nd ed., John Wiley and Sons, 1987.

[20] M. E. Cates, S. M. Fielding, Rheology of giant micelles, Adv. Phys. 55 (2006) 799–879.

[21] R. G. Larson, The Structure and Rheology of Complex Fluids, 1st ed., Oxford University Press, 1999.

[22] S. Manneville, Recent experimental probes of shear banding, Rheol. Acta 47 (2008) 301–318.

[23] J. F. Berret, Transient Rheology of Wormlike Micelles, Langmuir 7463 (1997) 2227–2234.

[24] T. J. Ober, J. Soulages, G. H. McKinley, Spatially resolved quantitative rheo-optics of complex fluids in a microfluidic device, J. Rheol. 55 (2011) 1127–1159.

[25] M. M. Britton, P. T. Callaghan, Shear banding instability in wormlike micellar solutions, Eur. Phys. B 7 (1999) 237–249.

[26] P. Galvosas, P. T. Callaghan, Fast magnetic resonance imaging and velocimetry for liquids under high flow rates, J. Magn. Reson. 181 (2006) 119–125.

[27] J. R. Brown, P. T. Callaghan, Changing micellar order, lever rule behavior and spatio-temporal dynamics in shear-banding

at the onset of the stress plateau, Soft Matter 7 (2011) 10472–10482.

[28] J.-B. Salmon, A. Colin, S. Manneville, Velocity profiles in shear-banding wormlike micelles, Phys. Rev. Lett. 90 (2003) 1–4.

[29] M. P. Lettinga, S. Manneville, Competition between shear banding and wall slip in wormlike micelles, Phys. Rev. Lett. 103 (2009) 248302:1–4.

[30] J. M. Adams, S. M. Fielding, P. D. Olmsted, The interplay between boundary conditions and flow geometries in shear banding: Hysteresis, band configurations, and surface transitions, J. Non-Newtonian Fluid Mech. 151 (2008) 101–118.

[31] M. A. Fardin, D. Lopez, J. Croso, G. Grégoire, O. Cardoso, G. H. McKinley, S. Lerouge, Elastic turbulence in shear banding wormlike micelles, Phys. Rev. Lett. 104 (2010) 178303.

[32] A. Groisman, V. Steinberg, Elastic turbulence in a polymer solution flow, Nature 405 (2000) 53 – 55.

[33] M. A. Fardin, T. J. Ober, V. Grenard, T. Divoux, S. Manneville, G. H. McKinley, S. Lerouge, Interplay between elastic instabilities and shear-banding: three categories of taylor-couette flows and beyond, Soft Matter 8 (2012) 10072–10089.

[34] C. Perge, M. A. Fardin, S. Manneville, Inertio-elastic instability of non shear-banding wormlike micelles, Soft Matter 10 (2014) 1450–1454.

[35] K. P. Jackson, K. Walters, R. W. Williams, A rheometrical study of Boger fluids, J. Non-Newtonian Fluid Mech. 14 (1984) 173–188.

[36] C. J. Pipe, N. J. Kim, P. A. Vasquez, L. P. Cook, G. H. McKinley, Wormlike micellar solutions : II . Comparison between experimental data and scission model predictions, J. Rheol. (2010) 881–913.

[37] Y. T. Hu, A. Lips, Kinetics and mechanism of shear banding in an entangled micellar solution, J. Rheol. 49 (2005) 1001–1027.

[38] L. Bécu, S. Manneville, A. Colin, Spatiotemporal dynamics of wormlike micelles under shear, Phys. Rev. Lett. 93 (2004) 018301:1–4.

[39] M. R. López-González, W. M. Holmes, P. T. Callaghan, Rheo-NMR phenomena of wormlike micelles, Soft Matter 2 (2006) 855–869.

[40] E. Miller, J. P. Rothstein, Transient evolution of shear-banding wormlike micellar solutions, J. Non-Newtonian Fluid Mech. 143 (2007) 22–37.

[41] Y. T. Hu, C. Palla, A. Lips, Comparison between shear banding and shear thinning in entangled micellar solutions, J. Rheol. 52 (2008) 379–400.

[42] Y .T. Hu, Steady-state shear banding in entangled polymers?, J. Rheol. 54 (2010) 1307–1323.

[43] P. Boukany, S. Q. Wang, Use of particle-tracking velocimetry and flow birefringence to study nonlinear flow behavior of entangled wormlike micellar solution: from wall slip, bulk disentanglement to chain scission, Macromolecules 41 (2008) 1455–1464.

[44] T. Yamamoto, K. Sawa, K. Mori, Velocity measurements for shear flows of CTAB/NaSal aqueous solutions between parallel plates, J. Rheol. (2009) 1347–1362.

[45] C. J. Dimitriou, L. Casanellas, T. J. Ober, G. H. McKinley, Rheo-PIV of a shear-banding wormlike micellar solution under large amplitude oscillatory shear, Rheol. Acta 51 (2012) 395–411.

[46] W. I. Yong, K. F. Wissburn, M. M. Denn, Effect of edge fracture on constant torque rheometry of entangled polymer solutions, Macromolecules 38 (2005) 9385–9388.

[47] S. J. Haward, G. H. McKinley, Stagnation point flow of wormlike micellar solutions in a microfluidic cross-slot device : Effects of surfactant concentration and ionic environment, Phys. Rev. E 031502 (2012) 1–14.

[48] M. A. Fardin, T. Divoux, M. A. Guedeau-Boudeville, I. Buchet-Maulien, J. Browaeys, G. H. McKinley, S. Manneville, S. Lerouge, Shear-banding in surfactant wormlike micelles: elastic instabilities and wall slip, Soft Matter 8 (2012) 2535–2553.

[49] N. Spenley, M. E. Cates, T. McLeish, Nonlinear rheology of wormlike micelles, Phys. Rev. Lett. 71 (1993) 939–942.

[50] L. Zhou, G. H. McKinley, L. P. Cook, Wormlike micellar solutions: III. VCM model predictions in steady and transient shearing flows, J. Non-Newtonian Fluid Mech. In press (2014).

[51] C. J. Pipe, T. S. Majmudar, G. H. McKinley, High shear-rate viscometry, Rheol. Acta 47 (2008) 62–642.

[52] M. J. Cromer, L. P. Cook, G. H. McKinley, Pressure-driven flow of wormlike micellar solutions in rectilinear microchannels, J. Non-Newtonian Fluid Mech. 166 (2011) 180–193.

[53] V. Sharma, G. H. McKinley, An intriguing empirical rule for computing the first normal stress difference from steady shear viscosity data for polymer solutions and melts, Rheol. Acta 51 (2012) 487–495.

[54] W. Cox, E. H. Merz, Correlation of dynamic and steady flow viscosities, J. Polym. Sci. 28 (1958) 619.

[55] C. J. Dimitriou, G. H. McKinley, R. Venkatesan, Rheo-PIV analysis of the yielding and flow of model waxy crude oils, Energy & Fuels 25 (2011) 3040–3052.

[56] P. Pakdel, G. H. McKinley, Elastic instability and curved streamlines, Phys. Rev. Lett. 77 (1996) 2459:1–4.

[57] M. A. Fardin, T. J. Ober, C. Gay, G. Grégoire, G. H. McKinley, S. Lerouge, Criterion for purely elastic Taylor-Couette instability in the flows of shear-banding fluids, Europhys Lett. 96 (2011) 44004.

[58] T. Gallot, C. Perge, V. Grenard, M.A. Fardin, N. Taberlet, S. Manneville, Ultrafast ultrasonic imaging coupled to rheometry: Principle and illustration, Rev. Sci. Instr. 84 (2013) 045107.

[59] D. Bonn, S. Rodts, M. Groenink, S. Rafai, N. Shahidzadeh-Bonn, P. Coussot, Some Applications of Magnetic Resonance Imaging in Fluid Mechanics: Complex Flows and Complex Fluids, Annu. Rev. Fluid Mech. 40 (2008) 209-33.

[60] P. Pakdel, G. H. McKinley, A. Oztekin, Rheological and geometric scaling of purely elastic flow instabilities, J. Non-Newtonian Fluid Mech. 67 (1996) 19–47.

[61] H. Wilson, J. M. Rallison, Instability of channel flow of a shear-thinning White-Metzner fluid, J. Non-Newtonian Fluid Mech. 87 (1999) 75–96.

Supplementary Material

Click here to download Supplementary Material: supp_info_casanellas.pdf